

# Analytical description of the structure of chaos

M. Harsoula, G. Contopoulos and C. Efthymiopoulos

Research Center for Astronomy and Applied Mathematics, Academy of Athens

**Abstract:** We consider analytical formulae that describe the chaotic regions around the main periodic orbit ( $x = y = 0$ ) of the Hénon map. Following our previous paper (Efthymiopoulos, Contopoulos, Katsanikas 2014) we introduce new variables  $(\xi, \eta)$  in which the product  $\xi\eta = c$  (constant) gives hyperbolic invariant curves. These hyperbolae are mapped by a canonical transformation  $\Phi$  to the plane  $(x, y)$ , giving "Moser invariant curves". We find that the series  $\Phi$  are convergent up to a maximum value of  $c = c_{max}$ . We give estimates of the errors due to the finite truncation of the series and discuss how these errors affect the applicability of analytical computations. For values of the basic parameter  $\kappa$  of the Hénon map smaller than a critical value, there is an island of stability, around a stable periodic orbit  $S$ , containing KAM invariant curves. The Moser curves for  $c \leq 0.32$  are completely outside the last KAM curve around  $S$ , the curves with  $0.32 < c < 0.41$  intersect the last KAM curve and the curves with  $0.41 \leq c < c_{max} \simeq 0.49$  are completely inside the last KAM curve. All orbits in the chaotic region around the periodic orbit ( $x = y = 0$ ), although they seem random, belong to Moser invariant curves, which, therefore define a "structure of chaos". Orbits starting close and outside the last KAM curve remain close to it for a stickiness time that is estimated analytically using the series  $\Phi$ . We finally calculate the periodic orbits that accumulate close to the homoclinic points, i.e. the points of intersection of the asymptotic curves from  $x = y = 0$ , exploiting a method based on the self-intersections of the invariant Moser curves. We find that all the computed periodic orbits are generated from the stable orbit  $S$  for smaller values of the Hénon parameter  $\kappa$ , i.e. they are all regular periodic orbits.

## 1. Introduction

In a previous paper (Efthymiopoulos et al. 2014) we explored the applicability of analytical formulae describing the asymptotic manifolds emanating from unstable periodic orbits in conservative 2D maps and in Hamiltonian systems of two degrees of freedom. Such formulae were found by the method of *hyperbolic normal form*. As it was shown by Cherry (1926), Moser (1956, 1958) and Giorgilli (2001) the method defines a *convergent* series transformation such that the dynamics close to a hyperbolic fixed point takes an integrable form. The associated integral has the form  $\xi\eta = c$ , where  $(\xi, \eta)$  are new canonical variables defined from the original variables by a convergent transformation. The value  $c = 0$  corresponds to the asymptotic manifolds emanating from the periodic orbit. The proof of the convergence is based on the fact that the hyperbolic normal form series do not contain terms with small divisors, in contrast with the corresponding series around a stable periodic orbit, which are in general only formal.

Applications of such series in simple mappings were made by da Silva Ritter et al. (1987), who gave the stable and unstable asymptotic curves up to a large extent by using high order truncations of the series. In particular they found a number of homoclinic points (i.e. intersections of the stable and unstable manifolds of the same periodic orbit). In the case of continuous Hamiltonian flows, Vieira and Ozorio de Almeida (1996), and Ozorio de Almeida and Vieira (1997) attempted to compute homoclinic orbits by purely analytical means. However, as we have shown in Efthymiopoulos et al. (2014), the domain of convergence of the hyperbolic normal form in the Hamiltonian case contains no homoclinic points (see also Bongini et al. (2001)). The limits of the domain of convergence can be associated with some singularities of the equations of the Hamiltonian flow in the complex time domain. However it is possible to overcome this problem (Efthymiopoulos et al. 2014) by a method of analytic continuation allowing to extend the computation of the asymptotic curves to an arbitrarily large length using only series. This allowed, in turn, the calculation of many homoclinic points. In general, the hyperbolic normal form lends itself quite conveniently to the computation of both homoclinic and heteroclinic points (i.e. intersections of the manifolds of different periodic orbits, see Contopoulos et al. 2013).

The asymptotic curves make an infinite number of oscillations passing close to the unstable periodic points but also extending to large distances from them. Thus, the asymptotic orbits, which start on these curves, go to large distances but return an infinite number of times close to the original periodic orbit. The successive points of intersection of an asymptotic orbit by a surface of section are distributed in an apparently random way on this surface, belonging to what is commonly referred to as the chaotic layer (or chaotic sea) around the unstable periodic orbit. However, the fact that the successive consequents of an asymptotic orbit can, in principle, be *all* computed by convergent series implies that these points are not truly randomly distributed, i.e., that there is some underlying ‘structure of chaos’. In the same way, the orbits with initial conditions close to the asymptotic ones also belong to invariant curves defined by the integral  $c$  for values  $c \neq 0$ . Thus, chaos is not only deterministic, but has a certain “structure” that can be defined by the form of the entire set of these invariant curves within the series’ domain of convergence.

In our first paper (Efthymiopoulos et al. 2014) we gave one example of an invariant curve with  $c \neq 0$  in a Hamiltonian model. However, we made no attempt to study such invariant curves in detail. This is done in the present paper, in which we discuss in detail the invariant curves  $c \neq 0$  in a case of the conservative 2D Hénon map with a hyperbolic point at the origin. Our aims are: i) to define with precision the domain of series convergence, ii) to discuss how the series truncation errors scale with truncation order, iii) to compute the forms of the invariant curves within this domain, and finally, iv) to study how these forms are related to particular features of the dynamics close to the hyperbolic point. Overall, we discuss both the benefits and the limitations of the method of hyperbolic normal form in characterizing the local ‘structure of chaos’ around hyperbolic points.

In section 2 we find a series transformation  $\Phi$  of the original variables  $(x, y)$  of the Hénon map around the unstable point  $(0, 0)$  in terms of new canonical variables  $(\xi, \eta)$ , in which the invariant curves are hyperbolae  $\xi\eta = c$ . These curves, and their maps to the original variables, are hereafter called ‘invariant Moser curves’, since their computation relies on the method presented in Moser (1956). We find that the transformation is convergent within the (approximate) limits  $|c| \leq 0.49$  and we study the accuracy of our calculations by varying the truncation order of the series and the value of  $c$ . We show that, for  $c$  close to zero, the invariant Moser curves lie completely outside the last KAM curve of a central island of stability on the  $(x, y)$  plane which exists at some distance from the hyperbolic fixed point. However, as  $c$  approaches the limiting value 0.49, there are invariant Moser curves intersecting, or even lying entirely within the island of stability. In section 3 we study the latter case in detail, and we explain why this causes no inconsistency with a different set of invariant curves, namely the KAM curves of the regular orbits inside the island of stability. Finally, we discuss how the structure of the invariant Moser curves can be used to characterize the ‘stickiness’ of the chaotic orbits with initial conditions near and outside the boundary of the island of stability. In section 4 we study how the self-intersections of the invariant Moser curves yield periodic orbits accumulating near the homoclinic points of the invariant manifold emanating from the central unstable periodic orbit. We show a numerical example of this accumulation. We also argue that all the periodic orbits found by such intersections are regular, i.e. they have been generated by bifurcations from the stable periodic orbit  $S$  at the center of the island of stability. Section 5 summarizes our conclusions.

## 2. Domain of Convergence

We consider the Hénon symplectic map (Hénon 1969) ‡

$$\begin{aligned} x' &= \cosh(\kappa)x + \sinh(\kappa)y - \frac{\sqrt{2}}{2}\sinh(\kappa)x^2 \\ y' &= \sinh(\kappa)x + \cosh(\kappa)y - \frac{\sqrt{2}}{2}\cosh(\kappa)x^2 \end{aligned} \quad (1)$$

with  $\kappa = 1.43$ , that was studied by da Silva Ritter et al. (1987). The origin  $(x = y = 0)$  is an unstable periodic orbit with eigenvalues  $\lambda_1 = e^\kappa \approx 4.1787$  and  $\lambda_2 = e^{-\kappa} = 1/\lambda_1 \approx 0.2393$ . Then we find a near identity canonical transformation  $\Phi = (\Phi_1, \Phi_2)$  of the form  $x = (u + v)/\sqrt{2}$ ,  $y = (u - v)/\sqrt{2}$  with

$$\begin{aligned} u &= \Phi_1(\xi, \eta) = \xi + \Phi_{1,2}(\xi, \eta) + \dots \\ v &= \Phi_2(\xi, \eta) = \eta + \Phi_{2,2}(\xi, \eta) + \dots \end{aligned} \quad (2)$$

‡ We call it Hénon map because of its similarity with the original Hénon map (1969), which has *sines* and *cosines* instead of hyperbolic *sines* and *cosines*. Da Silva Ritter et al. (1987) used the hyperbolic form of the Hénon map, but they missed a factor  $\sqrt{2}/2$  in their equation (17) that corresponds to our Eq. (1). Nevertheless their further equations are correct.

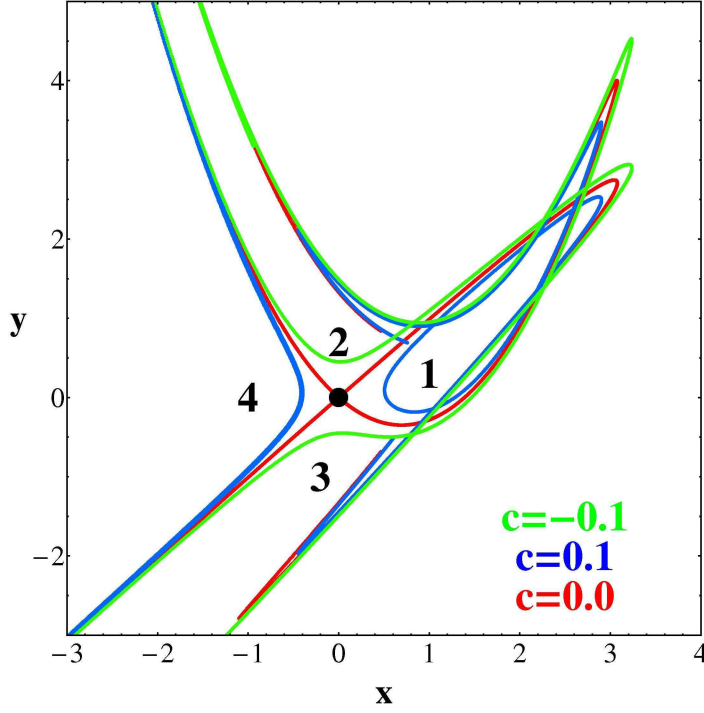


**Figure 1.** The asymptotic curves  $c = \xi\eta = 0$  (red, mapped in the original variables  $(x, y)$ ) from the unstable periodic orbit  $(x = y = 0)$  and the nearby invariant curves with  $c = 0.1$  (1 and 4), or  $c = -0.1$  (2 and 3).

where  $\Phi_{i,s}$  are polynomials of degree  $s$  in the new variables  $(\xi, \eta)$  such that the mapping (1) in the new variables takes the form

$$\begin{aligned}\xi' &= \Lambda(c)\xi \\ \eta' &= \frac{1}{\Lambda(c)}\eta\end{aligned}\tag{3}$$

with

$$c = \xi\eta = \text{constant}\tag{4}$$

and

$$\begin{aligned}\Lambda(c) &= \lambda_1 + w_2c + w_3c^2 + \dots \\ \frac{1}{\Lambda(c)} &= \lambda_2 + v_2c + v_3c^2 + \dots\end{aligned}\tag{5}$$

where  $w_s, v_s$  are constants. The details of how to compute the functions  $\Phi$  and  $\Lambda$  are given by da Silva Ritter et al. (1987).

The quantity  $c = \xi\eta$  is an integral of motion. The cases  $c = 0$  ( $\xi = 0$  or  $\eta = 0$ ) correspond to the stable and unstable manifold of the unstable periodic orbit  $(0, 0)$ . When mapped back to the plane of the original variables  $(x, y)$  by the functions  $\Phi$  of Eq.(2), the stable and unstable manifolds are curves intersecting each other at an infinite number of homoclinic points. Figure 1 shows the form of the stable and unstable

manifolds for the mapping (1) (red curves). Two computations are superposed: a purely numerical one, and an analytical computation using the transformation  $\Phi$  truncated at the order  $r = 100$ , but the two sets of curves are visually indistinguishable in the scale of Fig.1. An analysis of the error of the analytical method is discussed in detail below. Here, we only note that even low order truncations (e.g.  $r = 20$ , Da Silva Ritter et al. 1987) allow to find the first few homoclinic points. Efthymiopoulos et al. (2014) extended their results and found nine homoclinic points at the truncation order  $r = 60$ . Further homoclinic points can be found by higher order truncations. Note that, due to the particular form of the mapping (1), intersections of the asymptotic curves exist only on the right of the origin ( $x = y = 0$ ), while it can be easily shown that the curves on the left of the origin extend indefinitely to infinity and have no intersections.

Now, Fig.1 shows also some examples of invariant Moser curves for  $c \neq 0$  (blue and green curves). On the plane  $(\xi, \eta)$ , these curves are hyperbolae  $c = \xi\eta$ . We observe that the images of such hyperbolae in the variables  $(x, y)$ , for small  $|c|$ , are similar to the corresponding images of the curves  $c = 0$ . For example, the image of the curve  $c = 0.1$  (blue curve) on the right of the origin  $(0, 0)$  (region 1) follows closely some parts of the images of both curves  $\eta = 0, \xi > 0$  (unstable manifold) and  $\xi = 0, \eta > 0$  (stable manifold). Also, the image of the curve  $c = 0.1$  intersects itself close to the homoclinic points of the case  $c = 0$ . On the left of the origin there is another curve with  $c = 0.1$  (blue curve, region 4), that follows closely the curves  $\eta = 0, \xi < 0$  and  $\xi = 0, \eta < 0$ . This curve extends indefinitely to the left, upwards and downwards, without any intersections, in the same way as there are no homoclinic intersections along the images of the curves  $\eta = 0$  and  $\xi = 0$  on the left of the origin. Finally, in Fig.1 we plot also parts of the images of two curves with  $c = -0.1$  (green curves), one above the origin ( $x = y = 0$ ) (region 2) and another below the origin (region 3). Both curves approach the asymptotic curves, coming close to their homoclinic points.

The analytic representation of the invariant curves is successful within the domain of convergence of the series  $\Phi$  and  $\Lambda$ . We compute a numerical approximation of the boundary of the domain of convergence in the same way as in Efthymiopoulos et al. (2014). Namely, let us consider, for example, the series  $\Phi_1$ , which has the form

$$\Phi_1(\xi, \eta) = \sum_{r=1}^{\infty} \sum_{k=0}^r \Phi_{1,k,r-k} \xi^k \eta^{r-k} \quad (6)$$

with real coefficients  $\Phi_{1,k,r-k}$ . Let  $\phi$  be the angle of a fixed direction  $\phi = \tan^{-1}(\eta/\xi)$ . We write  $\xi, \eta$  in polar coordinates and we define the absolute sums:

$$g_{1,r}(\phi) = \sum_{k=0}^r \left| \Phi_{1,k,r-k} \cos^k \phi \sin^{r-k} \phi \right| \quad (7)$$

as well as a ‘d’Alembert sequence of radii’:

$$\rho_{1,r}(\phi) = \left( \frac{g_{1,r}(\phi)}{g_{1,r+2}(\phi)} \right)^{1/2} . \quad (8)$$

Assume that the limit

$$R_1(\phi) = \lim_{r \rightarrow \infty} \rho_{1,r}(\phi) \quad (9)$$

exists. Then, the series  $\Phi_1$  is analytic in the polydisk

$$D_{1,\phi} = \{|\xi| < R_1(\phi)|\cos(\phi)|, \quad |\eta| < R_1(\phi)|\sin(\phi)|\} \quad .$$

The complete domain of analyticity of the series  $\Phi_1$  around the origin is given by the union of polydiscs  $\mathcal{D}_1 = \cup_{0 \leq \phi < 2\pi} D_{1,\phi}$ . The intersection of the domain of analyticity  $\mathcal{D}_1$  with the real plane  $(\xi, \eta)$  has a limiting boundary defined parametrically as a function of  $\phi$  via the equations:

$$\xi = \xi_1(\phi) = R_1(\phi) \cos \phi, \quad \eta = \eta_1(\phi) = R_1(\phi) \sin \phi \quad . \quad (10)$$

In the same way we can determine a sequence of d'Alembert radii  $\rho_{2,r}(\phi)$  of the series  $\Phi_2$ , tending to asymptotic limiting values  $R_2(\phi)$  as  $r \rightarrow \infty$ . Figure 2a shows an example of the convergence of the d'Alembert sequence of radii  $\rho_{1,r}$  and  $\rho_{2,r}$  for the angle  $\phi = 3\pi/20$ . We observe that the convergence of both sequences  $\rho_{1,r}$  and  $\rho_{2,r}$  towards a limiting value is fast after approximately the order  $r = 20$ . Furthermore, we find  $\rho_{1,100} = 1.12$ ,  $\rho_{2,100} = 1.11$ , indicating that both sequences tend to approximately the same limiting value  $R_1(3\pi/20) \simeq R_2(3\pi/20)$ . In fact, we may use a numerical extrapolation technique to better estimate  $R_1$  or  $R_2$ . Namely, denote by

$$\delta\rho_{1,r} = \rho_{1,r} - R_1 \quad (11)$$

the sequence of differences between the  $r$ -th value of the d'Alembert sequence of radii  $\rho_{1,r}$  and the limiting value  $R_1$ . Using as an initial estimate  $R_1 \simeq \rho_{1,100}$ , we compute the differences  $\Delta\rho_{1,r} = \rho_{1,r} - \rho_{1,100}$  for  $r \ll 100$  (we set  $r < 50$  in the computation). Then, we numerically observe that, apart from a first few transient orders  $r$ , the sequence  $\Delta\rho_{1,r}$  scales approximately with  $r$ , up to  $r = 50$ , as a power-law, namely one finds that  $|\Delta\rho_{1,r}| \simeq \Delta_1 r^{-q}$ , where the constants  $\Delta_1, q > 0$  can be found by best-fitting. Assuming, now, that the estimate  $\delta\rho_{1,r} \approx \Delta_1 r^{-q}$  extends to all the true errors  $\delta\rho_{1,r}$  for  $r$  up to the maximum one, the sequence

$$\rho'_{1,r} = \rho_{1,r} - \Delta_1 r^{-q}$$

should be constant for large  $r$ . We then check numerically that  $\rho'_{1,r}$  is indeed constant to about three significant figures beyond  $r > 20$ . This allows to better estimate  $R_1$  as  $R_1 \simeq \rho'_{1,100}$ . Even more precise estimates can be obtained by iterating the above extrapolation algorithm. In the case of the data of Fig.2a, implementing the same algorithm to both sequences  $\rho_{1,r}$  and  $\rho_{2,r}$ , we find  $\rho'_{1,100} = 1.09554$ ,  $\rho'_{2,100} = 1.09555$ , indicating that  $R_1 = R_2 = R = 1.095$  with a precision of three significant digits.

The limiting value of  $R(\phi)$  defines the limiting point of Eq.(10). Repeating the computation for many different values of  $\phi$  in the interval  $0 \leq \phi < 2\pi$  allows to obtain a numerical approximation of the boundary of the domain of convergence. This is shown with a red curve in Fig.2b. The boundary is found to be hyperbola-like. In fact, computing  $c(\phi) = R^2(\phi) \cos(2\phi)/2$  with our numerical estimates of  $R(\phi)$  based on the extrapolation algorithm, we find that  $c(\phi)$  is *remarkably constant*, namely  $c(\phi) \simeq 0.49$  with a variation of less than  $3 \times 10^{-3}$  over the whole range of values of  $\phi$ . Note that, as shown in da Silva Ritter et al. (1987), one has  $R \rightarrow \infty$  in both limits  $\phi \rightarrow 0$  or  $\phi \rightarrow \pi/2$ ,

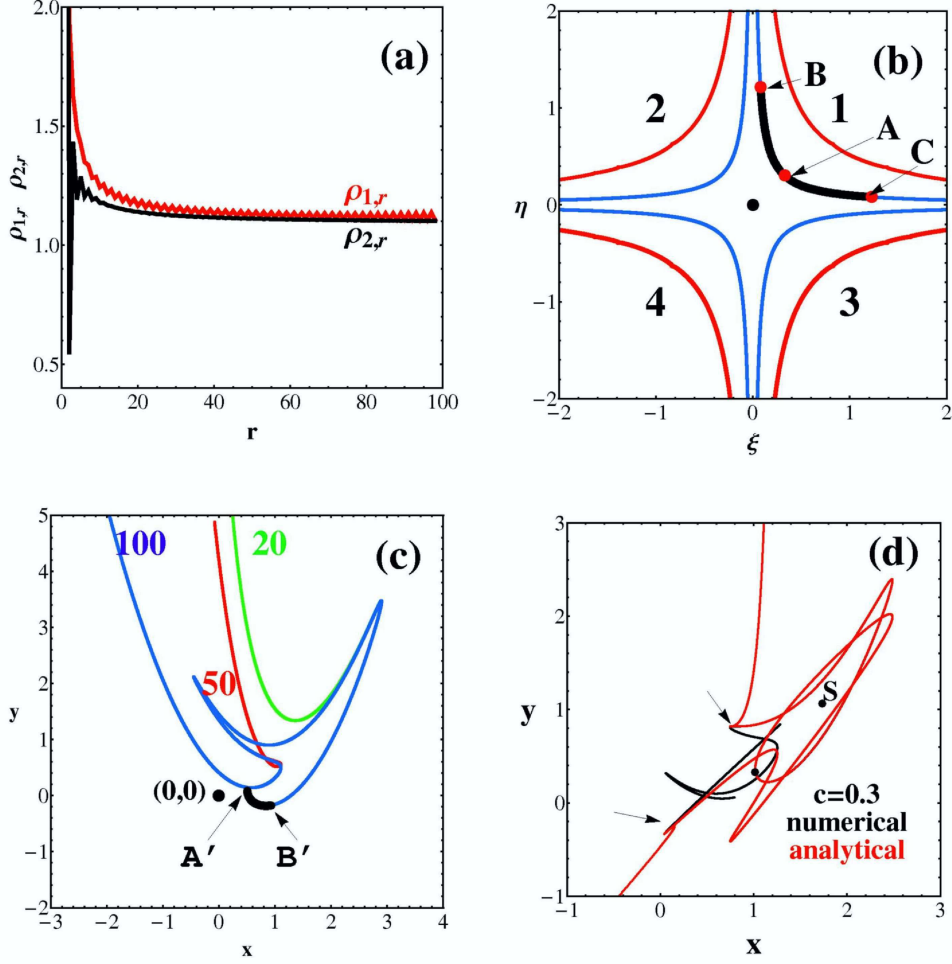


**Figure 2.** (a) The d'Alembert sequences of radii  $\rho_{1,r}$  (red) and  $\rho_{2,r}$  (black) for a particular direction with angle  $\phi = 3\pi/20$ . (b) The limiting hyperbola enclosing the region of convergence on the  $(\xi, \eta)$  plane corresponds to  $c \approx \pm 0.49$  (red curves). The invariant curves  $c = \xi\eta = \pm 0.1$  (blue curves) are well inside the limiting curves. The point  $A$  on the hyperbola  $c = 0.1$  has coordinates  $(\xi_A, \eta_A = \sqrt{c}, \sqrt{c})$ .  $B$  and  $C$  are its first images backwards and forward, respectively. (c) A comparison of the theoretical invariant curves  $c = 0.1$  by using series truncated at orders 20 (green), 50 (red) and 100 (blue). The accurate (numerical) invariant curve coincides with the blue curve. (d) Numerical (black) versus theoretical (red) invariant curves in the case  $c = 0.3$ . The theoretical curve using series truncated at order 100 deviates beyond the points indicated by arrows.

i.e., the domain of convergence extends to infinity along the  $\xi$  and  $\eta$  axes representing the invariant manifolds. For values of  $\phi$  very close to the limiting ones, 0 and  $\pi/2$ , the convergence of the d'Alembert sequences of radii is extremely slow. Even so, using the extrapolation algorithm yields the value  $c = 0.492$  even for  $\phi = \pi/2 - 1.57 \times 10^{-5}$ . In conclusion, after correcting with the extrapolation algorithm, our numerical evidence is that the boundary of the domain of convergence is very close to a hyperbola with  $c = c_{max} \simeq 0.49$  for all values of  $\phi$ . The same is true for the convergence of the series

$\Lambda(c)$  (Eq. (5)), where we have found, using d'Alembert sequences, that the boundary of the domain of convergence corresponds again to  $c = c_{max} \simeq 0.49$ .

Since the series  $\Phi$  are convergent for all  $(\xi, \eta)$  with  $|\xi\eta| < c_{max}$ , we may in principle use them to find the image, under  $\Phi$ , of all hyperbolae  $\xi\eta = c$  with  $|c| < c_{max}$ , in the plane  $(x, y)$ . However, in computing these images there arise practical limitations due to the errors by the use of only finite truncations of the series. A control of the error can be achieved by a combination of analytical and numerical propagation of the orbits, as exemplified in Figs.2b,c. In Fig.2c, the arc  $A'B'$  is the image under  $\Phi$  of an arc  $AB$ , shown in Fig.2b, which lies on the hyperbola  $c = 0.1$ . The point  $A$  is chosen in the diagonal, i.e.  $\xi_A = \eta_A = \sqrt{0.1}$ , while the point  $B$  is the first backward image of the point  $A$  under the normal form equations (3). In Figs.2b,c, both the point  $B$  as well as the image  $A'B'$  of  $AB$  were computed by taking the truncation of the series (3), (5) and (2), at the order  $r = 100$ . We can have an estimate of the truncation error by comparing the images of the arcs  $A'B'$  when computed at different truncation orders. We find that the differences between the images of the points of the arc  $A'B'$  at the orders  $r = 20$  and  $r = 60$  are about  $10^{-9}$  and between  $r = 60$  and  $r = 100$  are even smaller. Therefore, in the case  $c = 0.1$  the accuracy of the computed arcs  $A'B'$  truncated at order 100 is sufficient for further calculations.

We hereafter call the arcs  $AB$  (and their images  $A'B'$ ), ‘Moser arcs’, namely they are arcs belonging to an invariant Moser curve. Their main property is the following: if we iterate the Moser arc  $AB$  backwards using the inverse of the normal form equations (3), we obtain the whole upper branch of the invariant Moser curve  $c = 0.1$  from the point  $A$  upwards. In the same way, if we iterate the arc  $A'B'$  backwards using the inverse of the original Hénon mapping (Eqs.(1)), we obtain the image, under  $\Phi$ , of the upper branch of the Moser curve  $c = 0.1$  in the plane  $(x, y)$ . In the same way, we may obtain the image, under  $\Phi$ , of the lower branch of the invariant Moser curve  $c = 0.1$  from the point  $A$  downwards. Namely, we compute the Moser arc  $AC$ , where  $C$  is the first forward image of  $A$  under the Eqs.(3). Then, we use the series  $\Phi$  at a high truncation order to compute the image  $A'C'$  with accuracy, and then we propagate the arc  $A'C'$  forward using the original mapping equations (1).

The above process allows to find numerically the images, in the plane  $(x, y)$  under  $\Phi$ , of the whole Moser invariant hyperbolae for  $|c| < c_{max}$ . We call these curves ‘numerical’ or ‘exact invariant Moser curves’ (i.e. they are nearly free of series truncation errors). We notice that the ‘numerical’ or ‘exact’ curves cannot be defined independently of the mapping  $\Phi$ . The reason is that although the Hénon map (1) is exact and gives the iterate  $(x', y')$  of any given point  $(x, y)$ , only the rules of Eqs.(2), (5) and (3) allow to define an *invariant curve* (i.e. a curve mapped onto itself) joining the points  $A'$  and  $B'$  on the  $(x, y)$  plane. Furthermore, the whole computation relies on that the initial invariant arc  $A'B'$  should be possible to compute with precision via the arc  $AB$  using exclusively a high order truncation of the series  $\Phi$ .

On the other hand, we can also compute purely analytical images of the invariant Moser curves by implementing the (truncated) series  $\Phi$  directly to different points on the



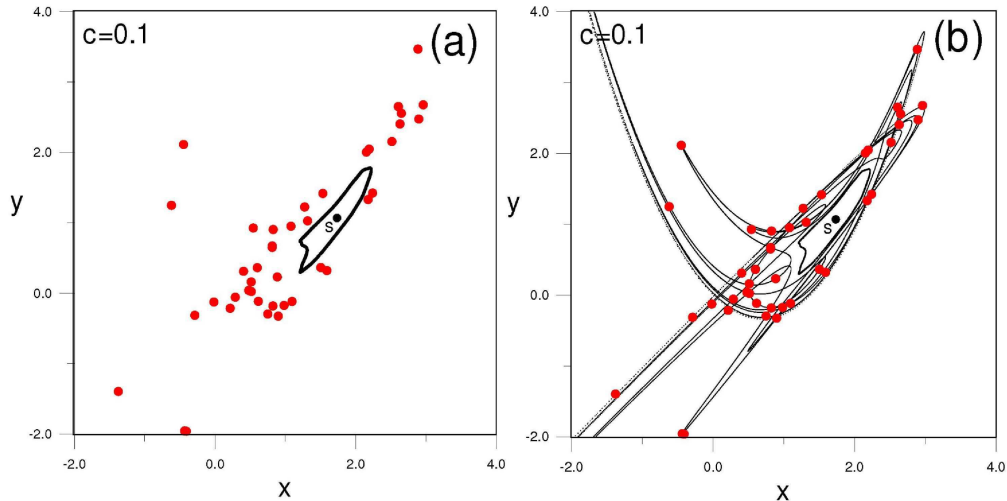


**Figure 3.** (a) The successive iterations of two orbits having initial points on the invariant curve  $c = 0.1$  seem to be distributed randomly around the last KAM curve of a central island of stability (b) The scattered points of Fig.3a belong in fact to the invariant curve  $c = 0.1$ .

hyperbolae *also outside* the arcs  $CAB$  (Fig.2b), i.e. without any numerical propagation. A comparison of the obtained images, for  $c = 0.1$ , at the truncation orders  $r = 20$ ,  $r = 50$ , and  $r = 100$  is shown in Fig.2c. We see that, using exclusively the series  $\Phi$  truncated at various orders, we find only parts of the ‘exact’ invariant curve, while beyond that part the theoretical curve deviates considerably. E.g. if we use series truncated at order  $r = 20$ , the deviation appears after the first oscillation (green curve). At the truncation order  $r = 50$  the deviation starts beyond the second oscillation (red curve). Finally, if we use series truncated at order  $r = 100$  we follow the exact curve well beyond the limit of applicability of the red curve, giving now also the third oscillation of the exact curve (blue curve).

Similar results are found for the initial arc  $A'C'$ , which is the image under  $\Phi$  of the arc  $AC$  of Fig.2b.

The accuracy decreases for larger (absolute) values of  $c$ . For example, in Fig.2d we compare the analytical invariant curve truncated at order 100 (red) for  $c = 0.3$  with the exact numerical curve (black) and we find large deviations after the second oscillation. For even larger  $c$ , close to the limit  $c = 0.49$ , the theoretical curve deviates even before the first oscillation of the exact curve.

If we compute the length  $s$  along an exact curve (around the point  $A'$ ) that is accurately represented by the analytical computation of the series up to the truncation order  $r$ , we typically find  $s \sim \log(r)$  (see also Efthymiopoulos et al. 2014). This estimate poses the overall limitations of the whole method of analytic (normal form) computations. Namely, the number of terms required to compute a part of fixed length  $s$  along an invariant Moser curve grows *exponentially* with  $s$ . This is consistent with the fact that these curves represent mostly chaotic motions. Namely, one requires an

exponentially growing amount of information (in the form, here, of series coefficients) in order to compute analytically larger and larger lengths of chaotic orbits. For example, Fig.3a shows some scattered points, which are successive iterates of two chaotic orbits with initial conditions on the invariant Moser curve  $c = 0.1$ . The thick curve represents the last KAM curve around an island of stability which surrounds a stable periodic orbit S at a certain distance from the origin. This last KAM curve plays a particular role, since it constitutes an absolute barrier separating orbits which lie entirely in the interior or the exterior of the curve. In particular, no chaotic diffusion leading to a crossing of the last KAM curve can occur. On the other hand, there are invariant Moser curves which intersect the last KAM curve. Thus, different initial conditions along one such invariant Moser curve lead in general to different orbits, which lie either entirely inside or entirely outside the last KAM curve. The connection between such invariant Moser curves and the behavior of orbits inside the island of stability will be discussed in section 3 below. The orbits of Fig.3a, instead, lie entirely outside the last KAM curve. A measurement of their Lyapunov characteristic exponents shows that these orbits are chaotic. The fact that the Lyapunov characteristic numbers are positive implies that successive iterates of points are far away from each other and appear as randomly scattered in a large neighborhood of the periodic orbit ( $x = y = 0$ ). However, in Fig.3b we see that all the scattered points belong to the same invariant Moser curve  $c = 0.1$ . Thus, in principle, these points can be found not only numerically but also analytically with sufficient accuracy by using the series  $\Phi$  at a high truncation order. Nevertheless, one needs to compute a  $\mathcal{O}(\exp N)$  number of terms in order to compute accurately the  $N$ -th iterate of each orbit. Thus, the orbits become practically non-computable beyond some iterations by using exclusively any reasonable order truncations of the series (2), (5) and (3).

Even so, the fact that these iterates are arranged along an invariant curve allows to define a ‘structure of chaos’, given by the ensemble of all the invariant Moser curves laying in the chaotic domain around the origin. This structure is important because it determines the dynamics of recurrences in the chaotic domain for all the orbits which do not belong to the asymptotic curves of the unstable periodic orbit at the origin (cf. Contopoulos and Harsoula 2008).

Using, now, the above method of ‘exact’ curves, in Fig.4 we plot the image, under  $\Phi$ , of the domain of convergence in the interior of the limiting boundary curves of Fig.2b. The corresponding region of convergence in the plane  $(x, y)$  is shown in red. The plot is obtained by computing the images of a foliation of hyperbolae for  $-c_{max} < c < c_{max}$ . The main remark is the following: the blue closed curve in the same plot is, again, the last KAM curve of the island of stability around the stable periodic orbit S at  $x \approx 1.736$ ,  $y \approx 1.065$ . We observe that, besides the chaotic domain around the origin, the region of convergence of the hyperbolic normal form series extends even *inside a part of the island of stability*. In particular, we find that there are invariant Moser curves intersecting, or even lying *entirely* within the interior of the last KAM curve. Let us note that by computing ‘numerical’ Moser curves for  $c$  very close to  $c = 0.49$  we find that these curves

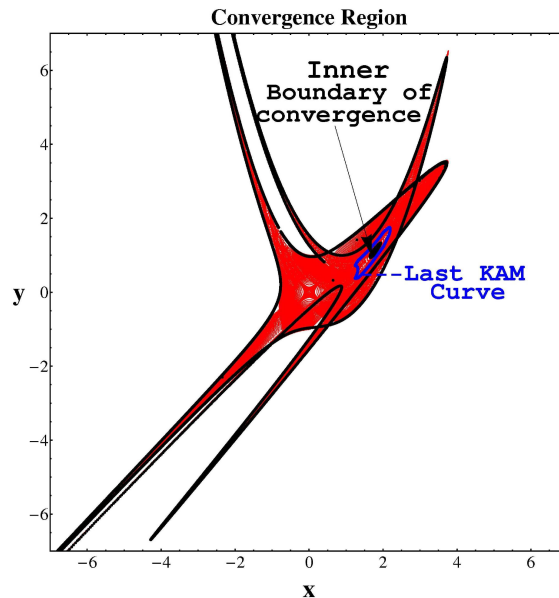


**Figure 4.** The region of convergence in the plane  $(x, y)$  corresponding to the image, under  $\Phi$ , of the region inside the limiting curves of Fig. 2b. The upper right limiting curve (1) of Fig. 2b is mapped into the island of stability, while the curves (2), (3), (4) are mapped into curves that surround the outer limits of the region of convergence. E.g. the line (2) is mapped into a curve that makes an infinite number of oscillations on the lower and upper side (most of them are close to the asymptotic curves from the periodic orbit  $(0, 0)$  on the left (upwards and downwards) and are not seen separately in this figure). A similar form is taken by the image of the curve (3), while the curve (4) is like a hyperbola without oscillations. The inner boundary of the region of convergence is inside the last KAM curve.

leave a small hole around the central elliptic fixed point, i.e., the domain of convergence does not reach the center of the central island of stability. Even so, the invariant Moser curves should be able to characterize not only chaotic motions, but also some features of the regular dynamics close to or inside the main island of stability. To this question we now turn our attention.

### 3. Island of stability - stickiness

In all computations of this section, the following conventions hold:

i) We refer to a ‘last KAM curve’ which is the same as the one shown in Fig.3a. This curve was computed by a detailed calculation of ‘rotation numbers’ and ‘twist numbers’, using a method developed by Voglis and Efthymiopoulos (1998).

ii) All invariant Moser curves were computed by the numerical method of the previous section, namely iterations of Moser arcs  $C'A'B' = \Phi(CAB)$  defined on the corresponding hyperbolae labeled by different values of  $c$ .

Since the last KAM curve is an absolute barrier separating its interior from the exterior under the mapping (1), it follows immediately that three cases can be

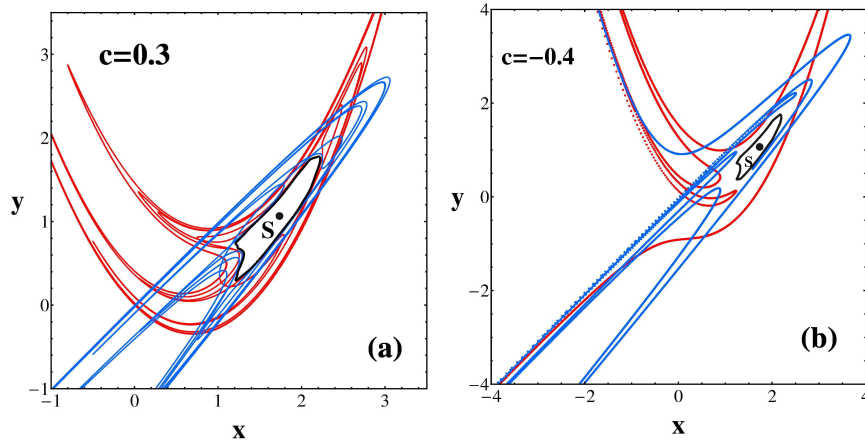


**Figure 5.** (a) The invariant curve  $c = 0.3$  fills most of the convergence region of Fig.4, outside the island of stability defined by the last KAM curve around the stable point  $S$ . (b) Two invariant curves with  $c = -0.4$  (blue and red) also fill most of the convergence region outside the island of stability  $S$ .

distinguished: a) an initial Moser arc  $C'A'B'$  lies entirely outside the last KAM curve. Then, every initial condition on this arc leads to an orbit lying entirely outside the last KAM curve. Thus, the *whole* corresponding invariant Moser curve lies entirely outside the last KAM curve. b) Similarly, initial Moser arcs lying entirely inside the last KAM curve define invariant Moser curves lying entirely inside the last KAM curve. However, if c) an initial Moser arc lies partly inside and partly outside the last KAM curve, then, by implementing the method described above, all initial points on the arc which are inside or outside the last KAM curve define two disjoint parts of the corresponding invariant Moser curve, which are inside and outside the last KAM curve respectively. Such curves play a role in the characterization of the phenomenon of ‘stickiness’, as will become clear by specific examples below.

As a first example, the numerical Moser curve  $c = 0.3$  fills most of the region of convergence of Fig.4 (Fig.5a). The backward images of the initial arc  $A'B'$  are given in red and the forward images of  $A'C'$  are given in blue. The higher arcs of the curve  $c = 0.3$  approach the last KAM curve (black curve) around the stable periodic point  $S$ . However as the initial arc  $C'A'B'$  lies outside the last KAM curve, its images cannot intersect the last KAM curve. This means that the whole invariant Moser curve  $c = 0.3$  is outside the last KAM curve. §

Similar invariant curves are formed when  $c < 0$ . In Fig.5b we plot the case  $c = -0.4$ . This curve also does not enter into the island  $S$  because its initial arc  $C'A'B'$  is far outside the last KAM curve.

On the other hand, the invariant curve  $c = 0.4$  does intersect the last KAM curve around  $S$  (Figs. 6ab), because the original arc  $C'A'B'$  of this curve intersects the last

§ Note the distinction of terminology: both The ‘KAM curves’ and the ‘Moser curves’ are invariant, i.e., they are mapped onto themselves under the mapping (1). However, as discussed in the text, their properties are different.

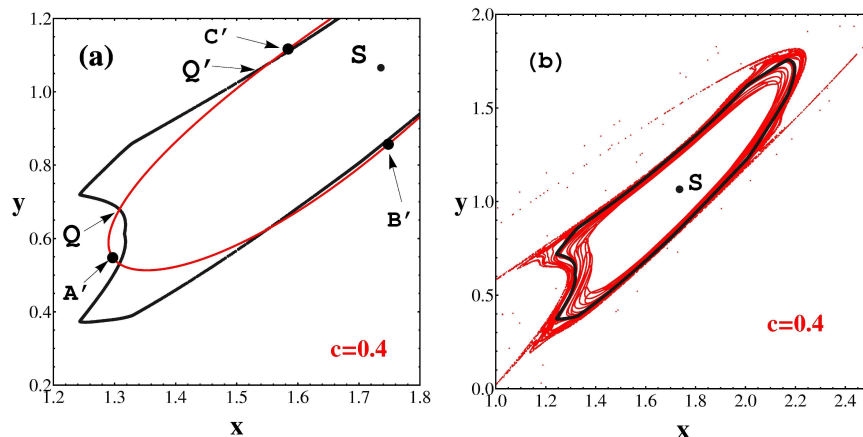


**Figure 6.** The invariant curve with curve  $c = 0.4$  (a) The initial arc  $C'A'B'$  of this curve intersects the last KAM curve. We note  $Q$  and  $Q'$  the points of intersection of the arc  $A'C'$  with the last KAM curve. (b) Further numerical images (using map (1)) of the initial arc  $C'A'B'$  of this curve extend to large distances outside the last KAM curve. Inside the last KAM curve they fill a region which is limited by another KAM curve.

KAM curve. In fact in Fig.6a we see 4 points of intersection. We note  $Q$  and  $Q'$  the points of intersection of the arc  $A'C'$  with the last KAM curve. The images of these points, infinite in number, are also points of intersection.

If we calculate numerically many iterations of the initial arc  $C'A'B'$  of the curve  $c = 0.4$  we find that part of it is inside the last KAM but it has also extensions outwards and probably it covers most of the region of convergence of Fig.4 (Fig.6b). On the other hand the curve  $c = 0.4$  enters also into the island of stability, therefore it intersects an infinity of closed KAM curves around  $S$ , inside the last KAM curve. Every point of the invariant curve  $c = 0.4$  inside the last KAM curve either belongs to a KAM curve or is between two KAM curves. The images of those points are also on KAM curves or between two KAM curves. Thus the initial arc  $C'A'B'$  of the invariant curve inside the last KAM curve has infinite images forming a ring around the point  $S$ .

Every KAM curve can be found exactly by means of analytic expressions around the central point  $S$  (KAM theorem). However the present theory of the Moser invariant curves (around the unstable point  $(0,0)$ ) is valid also between the KAM curves, where no expressions for KAM curves exist. The domain filled by the curve  $c = 0.4$  is a ring whose inner boundary is a limiting KAM curve (inside the last KAM curve, Fig.6b).¶

¶ In fact from the theory of the KAM curves (see, e.g., Contopoulos 2002) it is known that although the set of KAM curves has a positive measure there are infinitely many points between any two KAM curves not belonging to a KAM curve.

¶ It should be emphasized that there is no inconsistency between the fact that orbits with given initial conditions can be represented by two different types of convergent series. In fact, the hyperbolic normal form series converge in open domains of initial conditions, but their convergence is non-uniform along any particular KAM orbit. On the other hand the series of the KAM theory are convergent only on a Cantor set of initial conditions, even while their convergence along any particular KAM orbit is

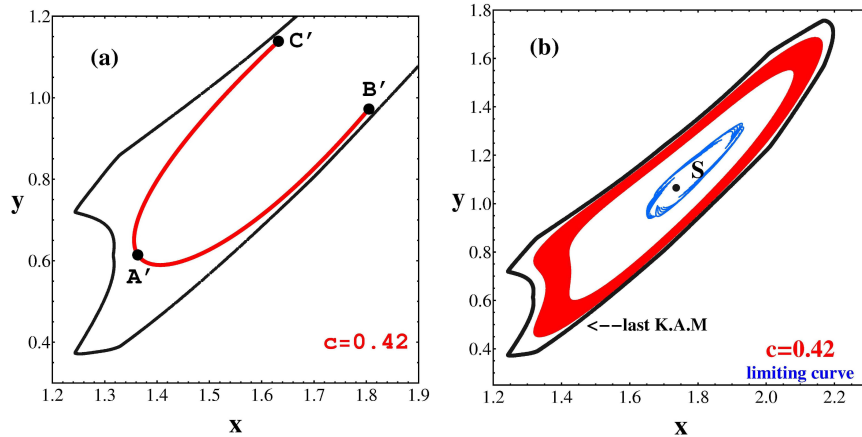


**Figure 7.** (a) The initial arc  $C'A'B'$  of the curve  $c = 0.42$  is marginally inside the last KAM curve (b) The curve  $c = 0.42$  fills a ring (red) completely inside the last KAM curve. The inner boundary of the region of convergence (blue) is very close to the invariant curve corresponding to the hyperbola with  $c = 0.49$ .

The transition between initial arcs  $C'A'B'$  of various "c" that are completely outside the last KAM curve and initial arcs that intersect the last KAM curve occurs close to  $c = 0.32$ .

If we increase  $c$  beyond  $c = 0.4$  we find cases in which the initial arc  $C'A'B'$  is completely inside the last KAM curve. Figure 7a is such a case for  $c = 0.42$ . Any other KAM curve passing through points of this initial arc has also infinitely many points of intersection with the images of the invariant Moser curve  $c = 0.42$ . Finally, the ring formed by this curve (red) if we take a large number of iterations of the initial arc  $C'A'B'$ , is limited on the outside and on the inside by KAM curves. In Fig.7b we also plot, for comparison, the region filled by the inner boundary of the convergence region (blue) which corresponds to  $c \approx 0.49$ .

It was shown above that the invariant Moser curves with  $c$  sufficiently close to the limiting value  $c_{max} = 0.49$  lie entirely within the main island of stability. As we decrease  $c$ , we find a critical value  $c_{crit}$  such that the invariant Moser curve with  $c = c_{crit}$  comes tangent with the last KAM curve surrounding the main island of stability. We find  $c_{crit} \simeq 0.41$  (compare Figs.6a for  $c=0.4$  and 7a for  $c=0.42$ ).

We now show how the properties of the invariant Moser curves in the neighborhood of the critical curve  $c = c_{crit}$  allow to characterize the *stickiness* of chaotic orbits with initial conditions outside, but close to the last KAM curve.

Consider two neighboring invariant curves with  $c_1 = c_{crit} + \epsilon$ ,  $c_2 = c_{crit} - \epsilon$ , for arbitrarily small  $\epsilon$  (positive). Since  $c_1 > c_{crit}$ , the invariant curve  $c = c_1$  lies entirely within the main island of stability. On the other hand, the endpoint of the initial arc  $A'C'$  along the curve  $c = c_2$  is located outside the last KAM curve. Let  $Q, Q'$  be the points where the initial arc along  $c = c_2$  intersects the last KAM curve (see for example uniform.

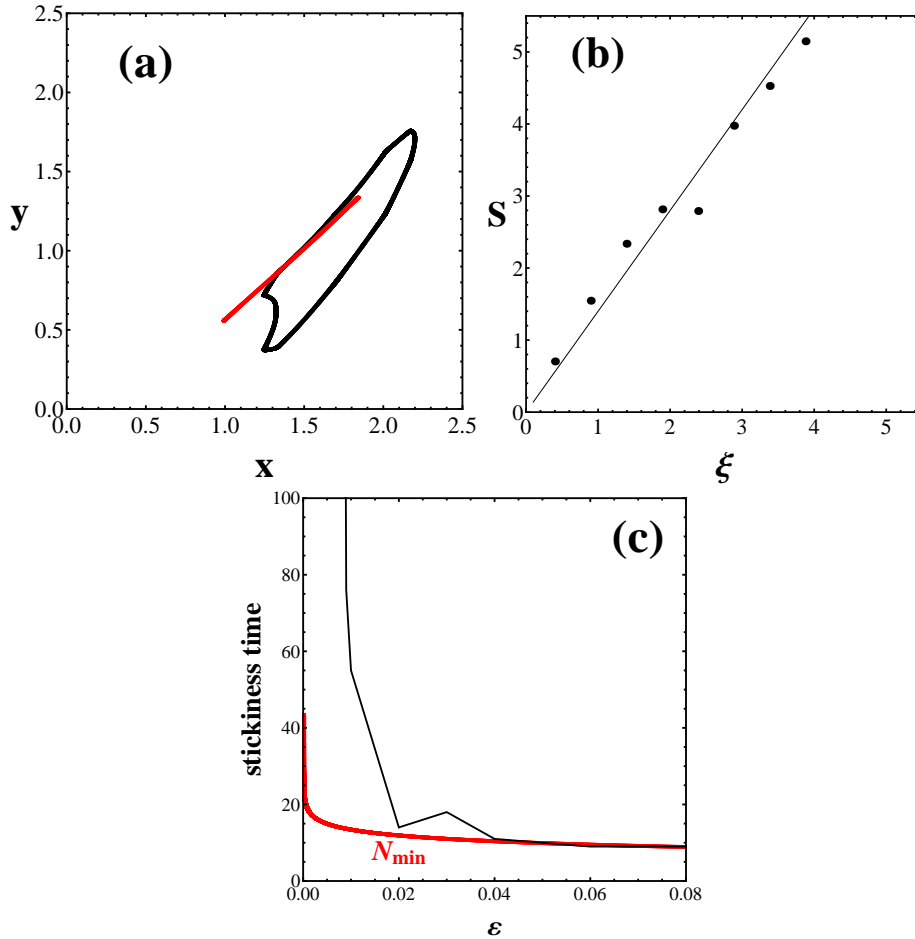


**Figure 8.** (a) The last KAM curve (black curve) together with the image, under  $\Phi$ , of a disc of size  $2.6 \times 10^{-6}$  centered on the hyperbola with  $c = c_{crit} = 0.41$  on the  $(\xi, \eta)$  plane (red curve). This is a very elongated ellipse of size about 1.1, i.e. of order unity. (b) The function  $S(\xi_0)$  of Eq. (11) is a power law of the form  $S(\xi_0) \sim 3.9\xi_0^{1.4}$ . (c) The prediction of the minimum stickiness time (red) against the true stickiness time (black) for initial conditions along invariant Moser curves with  $c = c_{crit} - \epsilon$  as a function of  $\epsilon$ .

Fig.6a, for  $c = 0.4$ ). Then, along the segments  $QA'$  and  $Q'C'$  there are some initial conditions whose images, after a (possibly large) number of iterations  $N$  under the mapping (1) can be far (at order unity distance) from the last KAM curve. We will now show that the above argument implies that the transformation  $\Phi$  has the following property: it is possible to find pairs of neighboring points  $(\xi_1, \eta_1)$  and  $(\xi_2, \eta_2)$ , separated by an arbitrarily small distance  $\delta$  in the plane  $(\xi, \eta)$ , whose images under  $\Phi$  are points  $(x_1, y_1)$  and  $(x_2, y_2)$  separated by an order unity distance.

Indeed, consider a point  $(\xi_{crit}, \eta_{crit})$  on the critical hyperbola with  $c = c_{crit}$ , as well as a disc  $\Delta$  centered on the point  $(\xi_{crit}, \eta_{crit})$  with radius  $\delta = \eta_1 - \eta_{crit}$ , where the point  $(\eta_1, \xi_{crit})$  with  $\eta_1 = c_1/\xi_{crit}$  belongs to the hyperbola with  $c = c_1$ . Then,  $\delta = (c_1 - c_{crit})/\xi_{crit} = \epsilon/\xi_{crit}$ . The points with constant  $\xi = \xi_{crit}$  and  $\eta$  between  $\eta_{crit}$

and  $\eta_1$  belong to hyperbolae with  $c > c_{crit}$ . Hence, they are mapped, under  $\Phi$ , to invariant Moser curves lying entirely within the last KAM curve. On the other hand, it is possible to find points with arbitrarily large  $\xi_2 = \xi_{crit}$ , i.e., arbitrarily small  $\delta$ , such that  $(x_2, y_2) = \Phi(\xi_2 = \xi_{crit}, \eta_2 = c_2/\xi_2)$  lies at an order unity distance from the last KAM curve. Then, the points  $(x_1, y_1) = \Phi(\xi_1 = \xi_2, \eta_1 = c_1/\xi_2)$  and  $(x_2, y_2)$  have order unity distance, despite the fact that  $(\xi_1, \eta_1)$  and  $(\xi_2, \eta_2)$  are  $\delta$ -close.

For  $\delta \rightarrow 0$ , the image under  $\Phi$  of a disc  $\Delta$  of radius  $\delta$  centered around some point  $(\xi_0, \eta_0)$  in the plane  $(\xi, \eta)$  is an ellipse in the plane  $(x, y)$  given by the quadratic form

$$(\Delta x, \Delta y) M^T M (\Delta x, \Delta y)^T = \delta^2 \quad (12)$$

where  $\Delta x = x - x_0$ ,  $\Delta y = y - y_0$ , with  $(x_0, y_0) = \Phi(\xi_0, \eta_0)$ , and  $M$  is the Jacobian matrix of the transformation  $\Phi$  evaluated at  $(\xi_0, \eta_0)$ . In fact, for  $\delta \rightarrow 0$  the linear approximation is valid. The semi-axes of the ellipse have size  $\delta/\sqrt{\mu_1}$ ,  $\delta/\sqrt{\mu_2}$ , where  $\mu_1, \mu_2$  are the eigenvalues of  $M^T M$ . The major semi-axis is  $s = \delta/\sqrt{\min(\mu_1, \mu_2)}$ . For a fixed hyperbola  $c = c_0$ , the quantity  $S = 1/\sqrt{\min(\mu_1, \mu_2)}$  can be expressed as a function of  $\xi_0$  only. If we set  $c_0 = c_{crit}$ , we can express the quantity  $s$  as a function of the coordinate  $\xi_0$  along the curve  $c = c_0$ , with  $\delta = \epsilon/\xi_0$  chosen so that the disc is limited between the hyperbolae  $c = c_1$  and  $c = c_2$ . We readily find

$$s(\xi_0, \epsilon) = \frac{\epsilon S(\xi_0)}{\xi_0}. \quad (13)$$

Equation (13) implies that, for  $\epsilon$  arbitrarily small, the distance  $s$  can become arbitrarily large, provided that  $S(\xi_0)$  grows with  $\xi_0$  *faster than linearly*. Figure 8 shows a numerical computation indicating that this is indeed the case in our numerical examples. Figure 8a shows the image, under  $\Phi$ , of a disc of size  $\delta \approx 2.6 \times 10^{-6}$ , centered around the point  $\xi_0 = 7600$ ,  $\eta_0 = c_0/\xi_0$ , with  $c_0 = c_{crit} = 0.41$ . Then,  $\epsilon = 0.02$ , i.e., the uppermost and lowermost points of the disc touch the hyperbolae  $c = 0.43$  and  $c = 0.39$  respectively. We see that the image  $\Phi(\Delta)$  is a very elongated ellipse whose most distant point from the center has a distance of order unity from the last KAM curve.

In order to compute the matrix  $M$  for the point  $(\xi_0, \eta_0)$ , we use a similar procedure as in section 2. Namely, we first compute the pre-image of  $\xi_0$  on the  $(\xi, \eta)$  plane by making a back transform for a number of  $n$  iterations using Eq.(3) so as to find the mapping  $\xi$  of  $\xi_0$  in the central region of Fig.2b. This value of  $\xi$  is of order unity. Then we can apply the truncated series  $\Phi$  in order to find the corresponding  $(x_0, y_0)$  point in the  $(x, y)$  plane. Finally we compute the  $N - th$  forward iterate of the numerical map (1). The matrix  $M$  is computed as the product of all the Jacobian matrices of the intermediate steps. This allows the computation of  $S(\xi_0)$ .

Repeating the process for  $n$  consecutive pre-images of  $(\xi_0, \eta_0)$  allows to obtain a numerical estimate of the form of the function  $S(\xi_0)$ . As shown in Fig.8b, this is fitted by a power-law of the form  $S(\xi_0) \sim S_0 \xi_0^p$ , with constant  $S_0 = 3.9$  and exponent  $p \approx 1.4$ . Thus,  $S(\xi_0)$  grows with  $\xi_0$  faster than linearly.

We now show that the above analysis allows to estimate a *minimum stickiness time* for the points  $A'$ ,  $C'$  of the initial Moser arc of the hyperbola  $c_2 = c_0 - \epsilon$ . Setting



$\xi_0 = c_0^{1/2} \Lambda(c)^N$  (for the  $N$ -th image of the point  $A'$ ), one has that  $S(\xi_0)$  becomes equal to  $S(\xi_0) = 1$  after a minimum number of iterations

$$N_{min} = -\frac{\log \epsilon + 0.5(p-1)(\log c_0) - \log S_0}{(p-1) \log \Lambda(c_0)} . \quad (14)$$

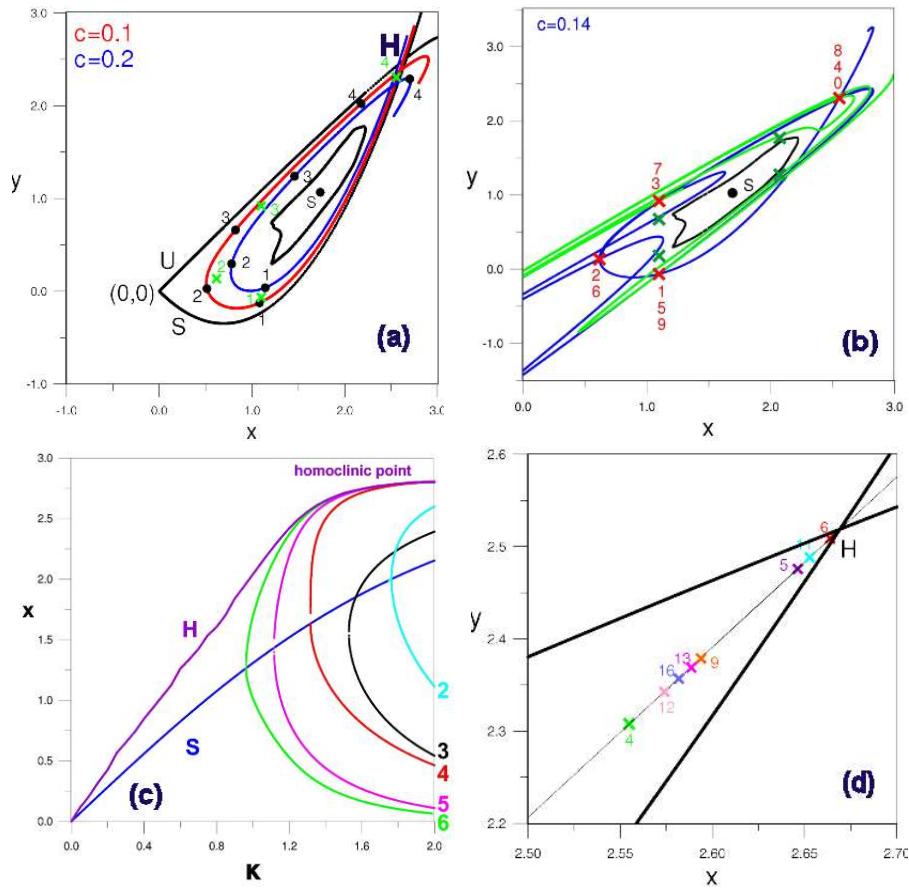
Note, that  $p > 1$  is a necessary condition for the stickiness effect, since only then  $N \rightarrow \infty$  as  $\epsilon \rightarrow 0$ .

Figure 8c shows a comparison between numerically obtained stickiness times (black curve) for initial conditions  $\xi_0 = \eta_0 = c^{1/2}$  with  $c = c_{crit} - \epsilon$ , as a function of  $\epsilon$ , along with the prediction of formula (14) (red curve) for the minimum stickiness time. We observe that the prediction actually represents the true stickiness time for  $\epsilon > 0.02$ . On the other hand, for  $\epsilon < 0.02$  the true stickiness time is substantially larger than the minimum stickiness time. In fact, this distinction is related to the existence of an 'inner' and 'outer' stickiness zone (see Contopoulos et al. 1997, Efthymiopoulos et al. 1997). In the inner stickiness zone, the stickiness time increases exponentially with  $1/\epsilon$ , thus it is much larger than the estimate of Eq.(14). We thus conclude that the estimates of the theory of invariant Moser curves predict qualitatively the stickiness phenomenon, but provide a useful quantitative estimate of the stickiness time only in the outer stickiness zone around an island of stability.

#### 4. Periodic orbits

For particular values of  $c$ , some self-intersections of the invariant Moser curves correspond to periodic orbits. As noted already by Birkhoff (1927, 1935), as  $c$  goes to zero, the periodic orbits lying on curves of smaller and smaller  $c$  accumulate to one or more homoclinic points, i.e., the points of intersection of the curves  $c = 0$ . Da Silva Ritter et al. (1987) computed numerically a number of unstable periodic orbits close to homoclinic points. An example of their method is shown in Fig.9a. We construct the invariant curves with  $c = 0.2$  (blue curve) and  $c = 0.1$  (red curve), up to points beyond their first self intersection, together with the case  $c = 0$  (black curve) that corresponds to the stable and unstable asymptotic curves of the unstable periodic orbit (0,0). The points of intersection are numbered 0 on each curve. Then we find the successive iterates, using the map (1), of the intersection points 0 along each curve. We see that along the curve  $c = 0.2$  the points 0, 1, 2, 3, 4 form more than one rotation around the center of the island S, while, along the curve  $c = 0.1$  the fourth iterate of 0 does not complete one full rotation. Therefore between the curves  $c = 0.2$  and  $c = 0.1$  there is an invariant curve along which the point 4 coincides with the original point 0. Expressing this last condition algebraically allows to compute the value of  $c$  by root-finding. We find  $c \simeq 0.14$ . Then, the point of intersection (0 or 4) is also found numerically. The four points 0, 1, 2, 3 represent a periodic orbit of period-4, shown by green crosses. The orbit has rotation number  $1/4$  around S.

If we continue the invariant curve for  $c = 0.14$  beyond the first passage from the point 0 (or 4) of self-intersection, the curve intersects itself at many more points. Most



**Figure 9.** (a) The asymptotic curves from the origin ( $U$  unstable and  $S$  stable) (black), the invariant curves  $c = 0.1$  (red) and  $c = 0.2$  (blue) and the last KAM curve around the stable periodic point  $S$ . The successive iterations of the intersection points on the curves  $c = 0.1$  and  $c = 0.2$  are marked with numbers from 1 up to 4. Between these two curves an unstable periodic orbit of multiplicity 4 lies on a curve  $c = 0.14$ , and is marked by green crosses (b) The invariant curve ( $c = 0.14$ ) (blue) passing through the 4 points 0, 1, 2, 3 (red crosses) of the periodic orbit of period  $-4$  (clockwise), This curve continues (as blue) through the point 4 (=0), 5 (=1), 6 (=3), 7 (=3), and then (as green) through 8 (=0), 9 (=1) etc. The second periodic orbit (green crosses) does not belong to this curve. (c) Characteristics of the central periodic orbit (blue curve) and of the families with rotation numbers  $1/2$ ,  $1/3$ ,  $1/4$ ,  $1/5$  and  $1/6$  bifurcating from it. The coordinate  $x$  of each periodic orbit is given as a function of the parameter  $\kappa$ . The position of the first homoclinic point  $H$  (intersection of the stable and unstable asymptotic curves) is marked as well. The various characteristics approach asymptotically the homoclinic curve as  $\kappa$  increases (d) Periodic orbits close to the homoclinic point  $H$  for  $\kappa = 1.43$ . All these orbits are close to a straight line and they are all regular.

of these self-intersections do not define periodic points (Fig. 9b). However, the curve passes also infinitely many times from the points 0,1,2,3 of the period-4 orbit (shown here with red crosses). In Fig.9b we see also a second period-4 periodic orbit (dark green crosses) which is unstable. This periodic orbit does not lie on the same invariant curve with  $c = 0.14$ , but it belongs to a different Moser curve.

In a similar way we find periodic orbits of rotation number  $1/5$ ,  $1/6$ , etc. It is obvious that there are infinitely many periodic orbits as we approach closer to the homoclinic point  $H$  (Fig.9c) of periods  $n = 4, 5, 6...$  having smaller and smaller rotation numbers around the stable orbit  $S$ . The homoclinic orbit itself can be considered as a limiting periodic orbit with infinite period and zero rotation number. All these orbits are generated by pitchfork bifurcations from the central periodic orbit, by varying the parameter  $\kappa$  of the mapping (1). Figure 9c shows the characteristic curves of the periodic orbits with  $n = 2$  to 6, along with the characteristic curve of the central stable orbit  $S$ . The position of the homoclinic point  $H$  as a function of  $\kappa$  is shown in the same plot, showing clearly how orbits of lower and lower  $n$  approach closer and closer to the homoclinic point  $H$  as  $\kappa$  increases.

Besides the periodic orbits with  $rot = 1/n$ , there are periodic orbits with  $rot = 2/n, 3/n$  etc. Such orbits were found by da Silva Ritter et al. (1987) by using the intersections of two or more Moser invariant curves. Between the orbits  $1/n$  and  $1/(n+1)$  we find orbits forming Farey trees, i.e. the orbits  $2/(2n+1)$ ,  $3/(3n+1)$ ,  $3/(3n+2)$ , etc. For  $\kappa$  sufficiently large, all these orbits are unstable and accumulate to the homoclinic point  $H$ . As shown in Fig. 9d, the points of intersection of the corresponding Moser curves are delineated approximately along a straight line.

A main empirical remark is now the following: we have checked that *all* the periodic orbits found by the intersections of the invariant Moser curves of the central unstable point  $O$  in the model (1) belong to the above category, i.e., they are generated by bifurcations from the stable central periodic orbit  $S$  and they form Farey trees as indicated above. In fact, all the periodic orbits given in Tables II and III of da Silva Ritter et al. (1987) belong also to the same category. Such orbits, generated by bifurcations from an initial orbit are called *regular* (see Contopoulos 2002). It is of interest to note that in this particular problem the lobes of the invariant manifolds of the central unstable point  $O$  cannot intersect themselves, thus they cannot generate irregular periodic orbits. This is due to the fact that on the left of the central unstable point  $O$  the asymptotic curves extend to infinity and the lobes on the right of these asymptotic curves cannot come back to intersect themselves.

On the other hand, in other cases where the asymptotic curves do not extend to infinity, there are irregular periodic orbits inside intersecting lobes (Contopoulos and Polymilis 1996, Contopoulos and Grousouzakou 1997). Thus, the possibility remains open that in other cases some intersections of one or more invariant Moser curves represent irregular periodic orbits. This subject is left for future study.

## 5. Conclusions

The Birkhoff-Moser normal form for a 2D symplectic mapping yields an integrable approximation of the mapping around an unstable equilibrium point, represented by a convergent series in a domain around the origin. Inside the domain of convergence, the dynamics takes, in new variables  $(\xi, \eta)$ , a simple form of a hyperbolic map:  $\xi' = \Lambda(c)\xi$ ,  $\eta' = \Lambda(c)^{-1}\eta$ , where  $c = \xi\eta = \xi'\eta'$  labels invariant hyperbolae. The function  $\Lambda(c)$  is given as a series in powers of  $c$ , while the mapping in the original variables  $(x, y)$  can be represented by a normalizing canonical transformation  $(x, y) = \Phi(\xi, \eta)$ . We studied in detail the convergence properties of the series  $\Phi$  and  $\Lambda$  in an example of the 2D symplectic Hénon map. The invariant manifolds of the unstable point  $(x, y) = (0, 0)$  are given by the images, under  $\Phi$ , of the axes  $\xi = 0$ ,  $\eta = 0$ , i.e.  $c = 0$ . However, in the present paper we focus on the properties of the curves corresponding to  $c \neq 0$ . In particular, we study the forms of these curves, as well as what they imply for the structure of chaos in the domain around the origin. Our main results are the following:

1) By using a simple numerical criterion of absolute convergence, we find numerical evidence that the limit of the domain of convergence of both series  $\Lambda$  and  $\Phi$  is close to a hyperbola with  $c = c_{max}$ , where, in our numerical example, we find  $c_{max} \simeq 0.49$ . We provide some estimates of the behavior of truncation errors, and propose an ‘extrapolation’ technique allowing to better determine the limit of the domain of convergence even when the truncation error of the series is relatively large.

2) The truncation error of the series is not uniform along an invariant curve with  $c < c_{max}$ . In general, at a fixed truncation order  $r$ , the error is minimum for the part of the hyperbola near the diagonal  $\xi = \eta$ , while it increases exponentially as  $\xi \rightarrow \pm\infty$  or  $\eta \rightarrow \pm\infty$ . Thus, in order to accurately represent a segment of the hyperbolae of length  $s$  around the diagonal in the original variables using the series  $\Phi$ , one needs to reach a truncation order  $r \sim \exp(s)$ . This implies the consistency of the series with the fact that they represent chaotic motions. Namely, in order to accurately determine more and more iterates of a chaotic orbit using the series, one needs to compute an exponentially increasing number of series terms.

3) Even so, one is able to obtain the form of the curves of constant  $c$  in the original variables  $(x, y)$  using a conjugation of the series with the mapping equations, as proposed in da Silva Ritter et al. (1987). In this way, we find the form of the domain of convergence as mapped in the original variables, as well as many other interesting properties of the Moser invariant curves. In particular, we find that beyond a critical value  $c = c_{crit} \simeq 0.41$ , the curves lie entirely within an island of stability around a stable periodic point  $S$ , at a distance from the (unstable) origin. The fact that we can have invariant curves of this type inside an island of stability does not contradict the existence of KAM curves. In fact, the curves of constant  $c$  represent the phase-mixing taking place along *open sets* of initial conditions both on KAM curves (regular) or on thin chaotic layers between the KAM curves (chaotic). However, the truncation error along the Moser invariant curves is non-uniform while along the KAM curves it is

uniform.

4) There are also curves  $c = \text{const}$  which lie entirely outside the last KAM curve of the island of stability, as well as curves  $c = \text{const}$  which intersect the last KAM curve. We compute the last KAM curve by a numerical criterion of ‘rotation and twist angles’ (Voglis and Efthymiopoulos 1998). We also consider the problem of how neighborhoods in the plane  $(\xi, \eta)$  are mapped into neighborhoods in the plane  $(x, y)$  for hyperbolae arbitrarily close (above and below) to the critical value  $c = c_{crit}$ . We demonstrate that the properties of the normalizing transformation  $\Phi$  imply a stickiness effect. Namely, initial conditions close to the diagonal for a curve with  $c = c_0 - \epsilon$ , with  $\epsilon > 0$  arbitrarily small, have a minimum stickiness time increasing with  $\epsilon$  as  $\sim -\log(\epsilon)$ .

5) For particular values of  $c$ , the curves  $c = \text{const}$  have self-intersections corresponding to periodic orbits of a predictable multiplicity. We compute such orbits, and, going to higher and higher multiplicity, we find how they accumulate close to homoclinic points of the invariant manifolds of the unstable fixed point at the origin. We find the bifurcation histories of these periodic orbits and show that they are all *regular*, i.e. belonging to Farey trees built by bifurcations around the stable fixed point at the center of the island of stability. In fact, taking into account the fact that in our mapping model some initial conditions lead to escapes, one can show that no irregular periodic orbits can be generated by the lobes of the invariant manifolds of the central unstable fixed point.

6) Finally, we emphasize the fact that, all the points of a chaotic orbit near the unstable periodic orbit of the origin  $(0,0)$ , although they seem to be distributed randomly, they belong in fact to particular ”Moser invariant curves”. Therefore, these curves define a ”structure of chaos”, which can be computed by analytical formulae inside the region of convergence.

## Acknowledgments

This work has been completed in the frame of the research project of RCAAM (Research Center for Astronomy and Applied Mathematics) ”Analytic computation of invariant manifolds and the structure of chaos”.

## References

- [1] Birkhoff, G.D., Acta Math. 50, 359 (1927)
- [2] Birkhoff G.D., "Nouvelles recherches sur les systèmes dynamiques", Memoriae Pont. Acad. Sci. Novi Lyncaei, ser. 3, Vol. I, 85 (1935)
- [3] Bongini, L., Bazzani, A. and Turchetti, G., Phys.Rev.Sp. Topics, **4**,114201 (2001)
- [4] Cherry ,T. M., Proc. London Math. Soc. Ser. 2, **27**, 151 (1926)
- [5] Contopoulos, G., "Order and Chaos in Dynamical Astronomy" *Springer* (2002)
- [6] Contopoulos, G. and Grousouzakou, E., Celest. Mech. Dyn. Astron, **65**, 33 (1997)
- [7] Contopoulos, G. and Polymilis, C., Celest. Mech. Dyn.Astron, **63**, 189 (1996)
- [8] Contopoulos, G., Voglis, N., Efthymiopoulos, C., Froeschlé C., Gonczi, R., Lega, E., Dvorak, R., Lohinger E., Celest. Mech. Dyn. Astron., **67**, 293 (1997)
- [9] Contopoulos, G. and Harsoula M., Int. J. Bif. Chaos, 18, 2929 (2008)
- [10] Contopoulos, G., Efthymiopoulos, C. and Katsanikas, M., 11th Hell. Astron. Conf., online at <http://www.hellas.gr/conf/2013/>, 26 (2013)
- [11] Da Silva Ritter, G.I., Ozorio de Almeida, A.M., & Douady, R., Physica D, 29, 181 (1987)
- [12] Efthymiopoulos, C., Contopoulos, G., Voglis, N., and Dvorak, R., J. Phys. A, **30**, 8167 (1997)
- [13] Efthymiopoulos, C., Contopoulos, G. and Katsanikas, M., Celest. Mech. Dyn.Astron., **119**, 331 (2014)
- [14] Giorgilli, A., Disc. Cont. Dyn. Sys., 7, 855 (2001)
- [15] Hénon, M., Quart. Appl. Math. **27**, 291 (1969)
- [16] Moser, J., Commun. Pure Applied Math., 9, 673 (1956)
- [17] Moser, J., Commun. Pure Applied Math., 11, 257 (1958)
- [18] Ozorio de Almeida, A.M. and Vieira, W.M., Phys. Lett. A, 227, 298 (1997)
- [19] Vieira, W.M., and Ozoiro de Almeida, A.M., Physica D, 90, 9 (1996)
- [20] Voglis, N. and Efthymiopoulos, C., J. Phys., A **31**, 2913 (1998)